Title

Hidden phonon highways promote photoinduced interlayer energy transfer in twisted transition metal dichalcogenide heterostructures.

Journal

Science Advances, 10(4)

Authors

Johnson, Amalya
Georgaras, Johnathan
Shen, Xiaozhe
et al.

Publication Date

2024-01-26

DOI

10.1126/sciadv.adj8819

Peer reviewed

APPLIED PHYSICS

Hidden phonon highways promote photoinduced interlayer energy transfer in twisted transition metal dichalcogenide heterostructures

Amalya C. Johnson[1]†, Johnathan D. Georgaras[1]†, Xiaozhe Shen[2], Helen Yao[1,2], Ashley P. Saunders[3], Helen J. Zeng[3], Hyungjin Kim[3], Aditya Sood[4]‡, Tony F. Heinz[2,4,5], Aaron M. Lindenberg[1,4,6], Duan Luo[1,2]*§, Felipe H. da Jornada[1], Fang Liu[3]*

Vertically stacked van der Waals (vdW) heterostructures exhibit unique electronic, optical, and thermal properties that can be manipulated by twist-angle engineering. However, the weak phononic coupling at a bilayer interface imposes a fundamental thermal bottleneck for future two-dimensional devices. Using ultrafast electron diffraction, we directly investigated photoinduced nonequilibrium phonon dynamics in MoS_2/WS_2 at 4° twist angle and $WSe_2/MoSe_2$ heterobilayers with twist angles of 7°, 16°, and 25°. We identified an interlayer heat transfer channel with a characteristic timescale of ~20 picoseconds, about one order of magnitude faster than molecular dynamics simulations assuming initial intralayer thermalization. Atomistic calculations involving phonon-phonon scattering suggest that this process originates from the nonthermal phonon population following the initial interlayer charge transfer and scattering. Our findings present an avenue for thermal management in vdW heterostructures by tailoring nonequilibrium phonon populations.

INTRODUCTION

Stacking atomically thin crystal layers into van der Waals (vdW) heterostructures (HSs) offers an exciting approach to create materials with unusual electronic, optical, and thermal properties beyond those of the constituent monolayers (*1*–*5*) and opens possibilities for promising applications in nanoelectronics, photonics, spintronics, and valleytronics (*6*–*12*). Heterobilayers based on transition metal dichalcogenides (TMDCs) are of particular interest, as they exhibit unique features of ultrafast interlayer charge transfer (CT) and a rich landscape of intra- and interlayer excitons (*3*, *4*, *13*–*18*), showing great potential for next-generation optoelectronic and excitonic applications (*4*, *11*, *12*, *19*, *20*). Moreover, the twist angle θ between the crystal lattice of adjacent layers in HSs provides an additional degree of freedom capable of further modulating their properties (*21*, *22*). The processes of charge carrier generation, transfer, recombination, and relaxation are strongly associated with phonon scattering and coupling (*23*–*28*). Phonons, as the main heat carriers in TMDCs, transport heat across the atomically sharp interface and hence determine the energy dissipation as well as thermal management in vdW HSs. A microscopic understanding of interfacial heat transfer and the management of nanoscale thermal transport is of utmost importance from both the fundamental and technological perspectives (*29*–*31*).

[1]Department of Materials Science and Engineering, Stanford University, Stanford, CA 94305, USA. [2]SLAC National Accelerator Laboratory, Menlo Park, CA 94025, USA. [3]Department of Chemistry, Stanford University, Stanford, CA 94305, USA. [4]Stanford Institute for Materials and Energy Sciences, SLAC National Accelerator Laboratory, Menlo Park, CA 94025, USA. [5]Department of Applied Physics, Stanford University, Stanford, CA 94305, USA. [6]Stanford PULSE Institute, SLAC National Accelerator Laboratory, Menlo Park, CA 94025, USA.
*Corresponding author. Email: fliu10@stanford.edu (F.L.); luoduan@opt.ac.cn (D.L.)
†These authors contributed equally to this work.
‡Present address: Department of Mechanical and Aerospace Engineering, Princeton University, Princeton, NJ 08540, USA; Princeton Materials Institute, Princeton University, Princeton, NJ 08540, USA.
§Present address: Key Laboratory of Ultra-fast Photoelectric Diagnostics Technology, Xi'an Institute of Optics and Precision Mechanics, Chinese Academy of Sciences, Xi'an 710119, China.

Many TMDC/TMDC HSs exhibit a type II band alignment (*32*, *33*), where their conduction band minimum and valence band maximum reside in opposite layers. Upon excitation of the HS by light, this alignment favors an interlayer CT, resulting in spatially separated but bound interlayer excitons. The interlayer CT has been reported to occur on a sub–100-fs timescale (*34*–*37*), independent of the interlayer twist angle (*35*, *37*). Several theoretical studies suggest phonon-mediated scattering plays a substantial role in the CT process via strongly hybridized intervalley excitons (*25*–*28*). However, despite considerable progress on the ultrafast CT in TMDC HSs, little work has been devoted to the photoinduced phonon dynamics in vdW HSs. This situation reflects the fact that conventional spectroscopic techniques, such as photoluminescence, transient absorption spectroscopy, and time- and angle-resolved photoemission spectroscopy, are not directly sensitive to phonon populations. By contrast, ultrafast electron diffraction (UED) is an ideal structural probe tool that allows direct measurement of real-time lattice dynamics with high temporal resolution and has been successfully applied to atomically thin two-dimensional (2D) materials (*38*–*42*). Recent UED studies on 15° WSe_2/WS_2 and MoS_2/graphene HSs revealed that the ultrafast transfer and scattering of charges in the HS leads to sub-picosecond, nearly simultaneous, heating of both layers at early times (*40*, *41*, *43*). These results illustrate the complex physical phenomena that can arise from the light-induced lattice dynamics of a 2D HS. Here, we use mega–electronvolt (MeV) UED to probe systematically the light-induced lattice dynamics in macroscopic type II TMDC heterobilayers formed between MoX_2 and WX_2 (X: S and Se), at various twist angles. By selective excitation of MoX_2 layer, we resolve real-time, layer-specific information of the heat exchange and thermalization process in the HSs.

RESULTS

The electron diffraction experiments were conducted using the MeV-UED facility at SLAC National Accelerator Laboratory (*44*, *45*). Figure 1A shows a schematic of the pump-probe UED experiment.

In brief, an ultrafast pump laser with a pulse duration of ~60 fs resonantly excites the A excitons of MoX_2. The type II band alignment allows holes to transfer from the MoX_2 to the WX_2 layer as shown in Fig. 1B, followed by phonon emission and transport between the layers. The layer-resolved lattice dynamics of the heterobilayer after photoexcitation are probed by diffraction using a ~150-fs, 4.2-MeV electron pulse. A few examples of static electron diffraction images of the monolayers and heterobilayers are shown in Fig. 1C. The large-area MoS_2, WS_2, $MoSe_2$, and WSe_2 monolayers were prepared using gold tape exfoliation (*46*), stacked at designed twist angles, and transferred to 10- to 15-nm-thick Si_3N_4 membrane window grids for Transmission Electron Microscopy (TEM). The twisted heterobilayers are uniform over the 250 μm–by–250 μm Si_3N_4 membrane (fig. S1). They allow clear identification of up to 10 orders of Bragg peaks in the diffraction images. The twist angles are determined by examination of the relative orientation θ between two sets of Bragg peaks, for which the actual twist angle between the two layers can be either θ or 60°-θ, due to symmetry. The optical absorption spectra for the monolayers (Fig. 1D) are used to identify the phonon energy required for resonant optical excitations. The samples are kept at cryogenic temperature (40 to 50 K) during the UED measurements.

When photoexcitation creates electrons and holes in TMDC vdW HSs, phonons will be emitted through electron-phonon coupling during charge carrier scattering and relaxation. After that, further heat exchange and thermalization will occur between the layers. Experimentally, the Bragg peak intensities decrease upon photoexcitation because of greater thermal motion of the atoms in the lattice (*47*). The Bragg peak intensities of different orders in $WSe_2/MoSe_2$ heterobilayers at different delay times t after photoexcitation are shown in Fig. 2 (A and B). Similar results for MoS_2/WS_2 is presented in fig. S3. The reduction in the Bragg peak intensity can be modeled with the standard Debye-Waller theory in a 2D lattice as

$$-\ln\left[\frac{I_{hk0}(t)}{I^0_{hk0}}\right] = \frac{1}{2}\Delta\langle u^2_{ip}(t)\rangle \cdot Q^2_{hk0} \quad (1)$$

Here, I^0_{hkl} and $I_{hk0}(t)$ are the integrated Bragg peak intensities at pump-probe delay times of $t < 0$ and t, respectively. Q_{hk0} is the reciprocal lattice vector of the relevant Bragg peak, and $\Delta\langle u^2_{ip}\rangle$ is the increase of the in-plane mean square displacement (MSD) of atoms from their equilibrium positions due to the induced disorder (*38*, *41*). A good linear fit of $-\ln\left[\frac{I_{hk0}(t)}{I^0_{hk0}}\right]$ versus Q^2_{hk0}, as shown in Fig. 2C ($WSe_2/MoSe_2$) and fig. S3 (MoS_2/WS_2), reflects the validity of this approach for our measurement conditions. Twice the inferred slope then yields the value of change in MSD, $\Delta\langle u^2_{ip}\rangle$. The evolution of the MSD as a function of time is obtained by fitting the data at each delay time t.

One example for atomic displacements in the $WSe_2/MoSe_2$ HS is shown in Fig. 2D. Upon resonant excitation of the $MoSe_2$ layer, the MSD of both layers rises immediately. At later times, the MSD falls due to heat dissipation into the underlying Si_3N_4 substrate and surrounding Si substrate, which act as heat sinks (*48*). The overall time-dependent MSD can be fitted correspondingly with a fast single-exponential rise and a multiexponential decay (convolved with the instrument response function). The detailed fitting procedure is described in the Supplementary Materials. Because the $MoSe_2$ layer is under direct photoexcitation, its lattice heats up very rapidly through efficient electron-phonon interactions. The time constant τ_1 for this prompt rise is 1 ps or shorter, which is also in good agreement with previously reported UED measurements of TMDC monolayers and bilayers (*38*, *40*, *41*, *43*, *49*). We observe a similar rapid rise for photoexcitation of isolated $MoSe_2$ and WSe_2 monolayers (Fig. 2E).

In contrast to the sub-picosecond lattice heating in the $MoSe_2$ layer, the MSD in the WSe_2 layer of the heterobilayer exhibits an additional, slower component of growth. The heat flowing into the WSe_2 layer has contributions from: (i) ultrafast interlayer hole transfer from $MoSe_2$ to WSe_2, creating phonons through electron-phonon coupling: This is expected to occur on the sub-picosecond timescale, as verified by earlier experimental results and first-principles calculations (*40*, *41*, *43*); (ii) weak optical absorption in

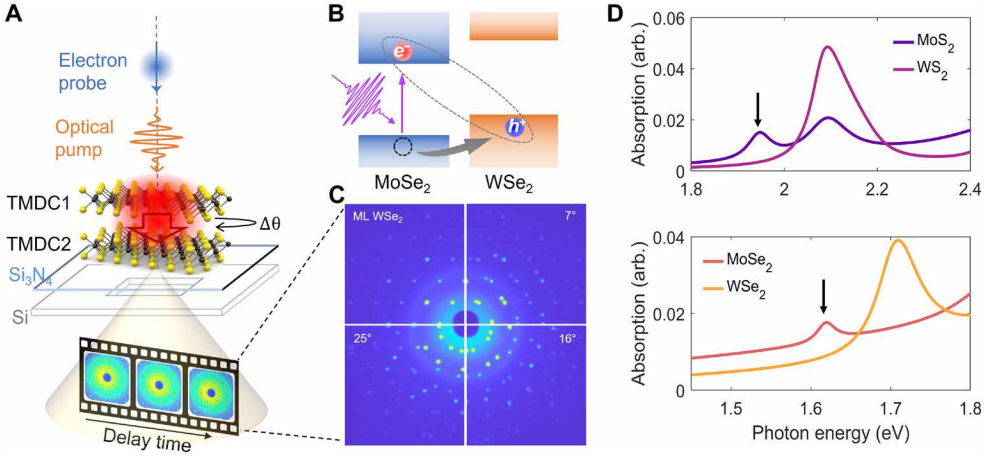

Fig. 1. Overview of UED setup. (**A**) Schematic representation of the femtosecond optical pump, electron probe experiment, recording lattice dynamics of a TMDC heterostructure on a Si_3N_4 membrane. (**B**) Band alignment and carrier transfer for the type II heterobilayers excited on resonance with the MoS_2 or $MoSe_2$ A exciton. (**C**) Static diffraction image of the WSe_2 monolayer (ML) and $WSe_2/MoSe_2$ heterobilayer with twist angles of 7°, 16°, and 25°. (Diffraction images for the other monolayers and heterobilayers are shown in fig. S2.) (**D**) Optical absorption of TMDC monolayers at 50 K. Top: MoS_2 (purple) and WS_2 (pink). Bottom: $MoSe_2$ (red) and WSe_2 (orange). The absorption spectra were obtained from fitting reflection contrast spectra. Arrows indicate the photon energy of the A exciton resonance of MoS_2 (1.93 eV) and $MoSe_2$ (1.62 eV).

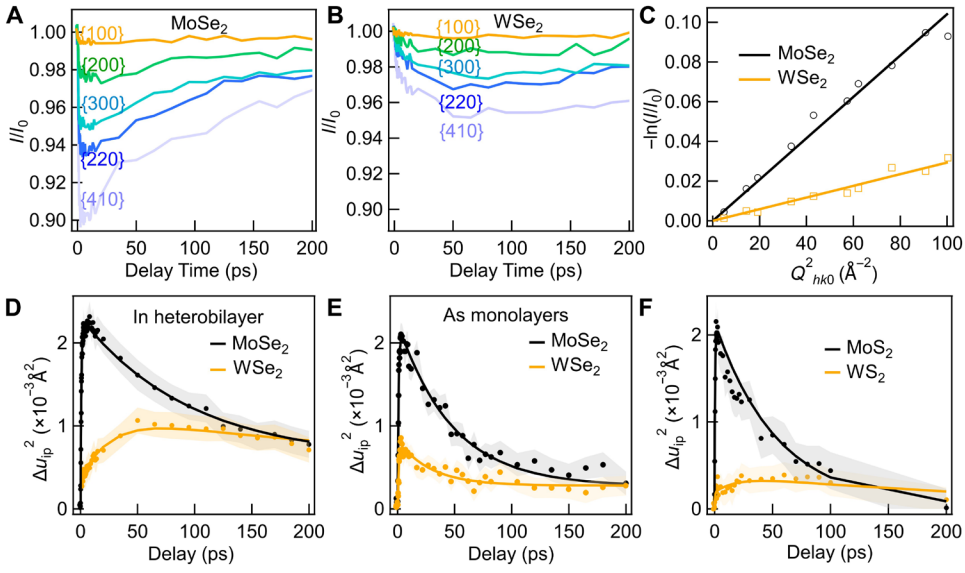

Fig. 2. Layer-resolved Debye-Waller response. (**A** and **B**) Integrated Bragg peak intensities as a function of pump-probe delay time for different orders of Bragg peaks in the $MoSe_2$ and WSe_2 layers of a 25° $WSe_2/MoSe_2$ heterobilayer. The heterobilayer pumped on resonance with the $MoSe_2$ A exciton with a fluence of 1 mJ/cm^2. Ten different diffraction orders were used in the analysis. To avoid congestion, five representative diffraction orders are shown. Bragg order indexes and corresponding Q^2_{hk0} are listed in table S1. (**C**) Log intensity change for different orders of Bragg peaks at delay time of 12 ps, plotted against the reciprocal lattice vector of the Bragg peak squared, with the corresponding linear fit of the Debye-Waller model. (**D**) Mean square displacement (MSD) of the WSe_2 and $MoSe_2$ in the heterobilayer as a function of delay time. The solid lines are fit curves, and shaded area represents uncertainty. (**E**) MSD of isolated WSe_2 and $MoSe_2$ monolayers under the same optical pumping conditions. (**F**) MSD of layers in a 4° MoS_2/WS_2 heterobilayer as a function of delay time, pumped on resonance with the MoS_2 A exciton under similar experimental conditions.

the tail of the WSe_2 A exciton peak: This contribution should also lead to sub-picosecond response, as seen in isolated WSe_2 monolayer in Fig. 2E; and (iii) interlayer heat transfer from $MoSe_2$ through anharmonic phonon-phonon interactions, which may occur at longer times.

In keeping with this discussion, the time-dependent MSD of WSe_2 plotted in Fig. 2D was fit with two different exponential rise components with fast (τ_1) and slow (τ_2) time constants. The fast rise τ_1 for WSe_2 layer is ~0.5 to 1 ps, similar to that of the $MoSe_2$ layer and of the isolated WSe_2 monolayers. This time constant is consistent with previous reports of the WS_2/WSe_2 HS, which revealed almost simultaneous heating of both layers in the HS, facilitated by the ultrafast interlayer CT (*40*, *41*, *43*). In contrast, the longer time constant τ_2, which reflects the process of the WSe_2 layer gaining additional energy from the adjacent photoexcited $MoSe_2$ monolayer, is on the order of 10 to 30 ps. This slow thermal heating channel is unique to the WSe_2 in a heterobilayer and is not observed in isolated monolayers. Similarly, we also identify a slow heating channel for the WS_2 layer in MoS_2/WS_2 heterobilayers, arising from heat flow from the photoexcited MoS_2 layer (shown in Fig. 2F).

The dependence of interfacial thermal transfer on different twist angles is important for elucidating the light-induced thermal dynamics in TMDC heterobilayers, especially those within moiré structures. Figure 3A shows the normalized MSD of the WSe_2 layer in $WSe_2/MoSe_2$ HSs at twist angles of 7°, 16°, and 25° and in WSe_2 monolayers. The corresponding values of τ_1 and τ_2 are shown in Fig. 3B. Among the tested samples with different twist angles, the time constant τ_2 of the WSe_2 layer appears slightly longer in the 16° and 25° heterobilayers compared with that in the 7° heterobilayer. This suggests a slower interlayer thermal energy transfer rate as the twist-angle mismatch increases. On the other hand, the fast response τ_1 remains 1 ps or less in the $MoSe_2$ and WSe_2 layers for all the HSs with different twist angles.

A layer-projected density functional theory (DFT) calculation of the electronic band structure of a $MoSe_2/WSe_2$ heterobilayer is displayed in Fig. 3C, showing the expected type II band alignment (see the Supplementary Materials). After resonantly exciting the $MoSe_2$ A exciton, the exciton-bound holes at the *K* and *K′* valleys scatter to layer-hybridized states around the Γ valley. Eventually, the holes scatter back to the *K* and *K′* valley states localized in WSe_2, forming interlayer excitons (*8*, *43*, *50*). Overall, this interlayer CT occurs on the order of a few tens of femtoseconds (*24*, *26*, *51*), independent of twist angles (*8*, *37*). The scattering and energy relaxation of holes will create an initial distribution of phonons in both the $MoSe_2$ and WSe_2 layers, resulting in a sub-picosecond rise of the MSD. Experimentally, we measured a sub-picosecond τ_1 in both heterobilayers and monolayers.

Throughout the ultrafast charge creation, relaxation and transfer between the two layers, any asymmetry in the phonon emission will lead to a temperature asymmetry between the layers. Such an interfacial temperature asymmetry would lead to a subsequent heat transfer between the layers, which explains the slower heating (τ_2 time constant) of WSe_2 seen in our experiments. To gain a microscopic understanding of the heat transfer process and obtain a quantitative assessment of the temperature in our experiments, we perform a series of atomistic calculations. We first performed molecular dynamics (MD) simulations using first-principles–parameterized empirical force fields with the Large-scale Atomic/Molecular Massively Parallel Simulator (LAMMPS) code (see the Supplementary Materials) (*52*). These simulations on $MoSe_2/WSe_2$ heterobilayers reveal the expected linear relationship between each layer's

temperature and its MSD (fig. S4) and predict peak temperatures in our experiments close to 100 K immediately after the $MoSe_2$ layer is optically pumped. While such classical calculations overestimate the interfacial thermal boundary conductance by using classical phonon statistics, the timescale associated with the heat conductance is often qualitatively well-described within a classical picture (*53*).

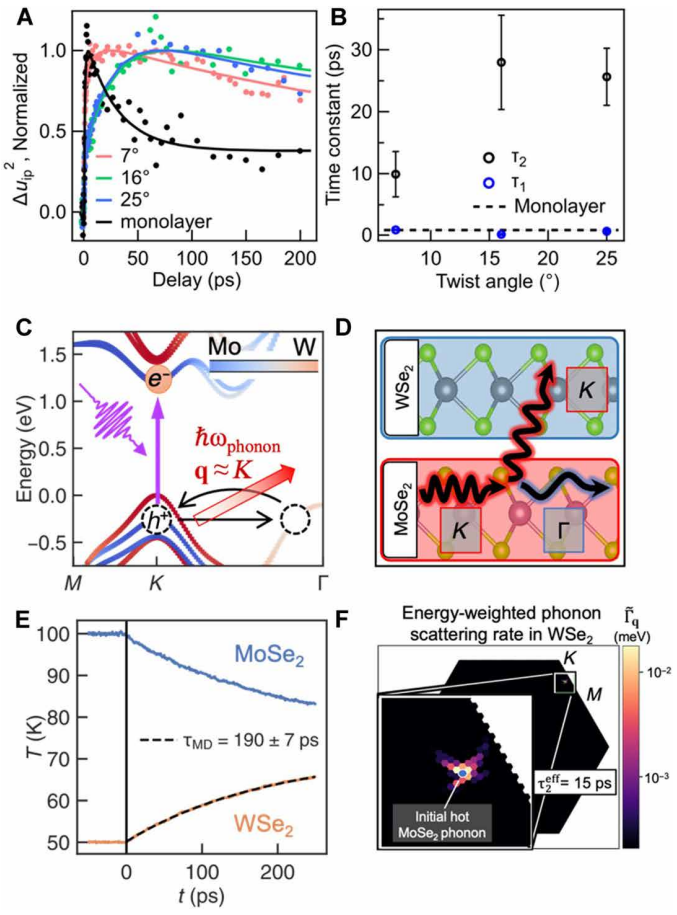

Fig. 3. Interlayer phonon scattering. (**A**) MSD of the WSe_2 layer in $WSe_2/MoSe_2$ HSs with twist angles of 7° (red), 16° (green), and 25° (blue) and of the WSe_2 monolayer (black). The MSD curves are normalized to their maximum fit values to aid in visualizing the different rise dynamics across samples. (**B**) Inferred values for the fast (τ_1, blue) and slow (τ_2, black) rise time constants for WSe_2 in the HS as a function of twist angles. The black dashed line represents τ_1 of the monolayer. (**C**) Layer-projected electronic band structure of a $MoSe_2/WSe_2$ HS showing a type II band alignment. After resonantly exciting the $MoSe_2$ A exciton, the exciton-bound holes at the *K* and *K*′ valleys scatter to layer-hybridized states around the Γ valley by emitting phonons with wave vectors close to *K* or *K*′. Eventually, the holes scatter back to the *K* and *K*′ valley states localized in WSe_2. (**D**) Diagrammatic representation of the fission-like interlayer phonon scattering. A higher-energy *K* wave vector phonon in the $MoSe_2$ layer decays into two lower-energy phonons: a lower energy near-Γ wave vector acoustic phonon (blue) in the $MoSe_2$ layer and a higher energy near-*K* wave vector acoustic phonon in the adjacent WSe_2 layer (red). (**E**) Interlayer thermalization time from MD simulations assuming each layer is individually in a local thermal equilibrium. (**F**) Brillouin zone (BZ)–resolved thermal scattering rate computed for the fission diagram in (D). Weighted scattering rate $\tilde{\Gamma}_{\mathbf{q}}$ are calculated as the fraction of energy transferred from the initial $MoSe_2$ phonon with wave vector **q** lying between *K* and *M* (the blue dot at the center of the inset) to various phonons on WSe_2 (the $\mathbf{q} \rightarrow 0$ acoustic phonon left behind on $MoSe_2$ is not shown).

We first assume that each layer in the heterobilayer system is individually in a local thermal equilibrium and subsequently let the system reach its global thermal equilibrium, as shown in Fig. 3E. On the basis of these assumptions, we deduce an interlayer thermalization time τ_{MD} between 190 and 350 ps. The timescale is consistent with thermalization time estimated from the previously reported TMDC interfacial thermal conductivities (*43*). However, it is about one order of magnitude longer than that τ_2 measured from experiments. The computed thermalization times also display a weak dependence on the twist angles we considered, from 7° to 25° (fig. S5). For the smaller twist angles where moiré structures are prominent, our simulations were not large enough to capture the large-scale relaxation domains and soliton formations.

To gain a deeper understanding of the limitations of the initial simulations, which assumed that the two layers were thermalized subsystems, it is important to consider the strict phase space constraints associated with the decay path of excited electrons and holes. As a result, the initially created phonons are restricted to crystal momenta close to a few high symmetry points in the Brillouin zone (BZ) (*51*, *54*). The momentum-dependent electron-phonon interactions and specific inelastic electron-phonon scattering pathways for hot carrier relaxation lead to a profoundly nonequilibrium phonon state with anisotropic momentum distribution. In particular, when the excited holes of $MoSe_2$ at the *K* and *K*′ valleys scatter to the regions around the Γ valley, primarily acoustic phonons are emitted whose wave vectors $\mathbf{q} \approx K$ form a ring around *K* in momentum space. This can be understood in terms of energy-momentum conservation arguments (*43*). Such phonons are localized in the $MoSe_2$ layer where the initial hole resides (see the Supplementary Materials). This mechanism is universal for different stackings of TMDC heterobilayers (*8*, *24*), leading to a nonthermal phonon distribution.

This nonequilibrium state may persist for a certain duration after photoexcitation. Prior UED and diffuse scattering experiments have shown that the phonon distribution of MoS_2 monolayers remains anisotropic within the initial 5 ps following photoexcitation (*39*). In addition, first-principles calculations of the electron-phonon and phonon-phonon interactions in monolayer MoS_2 revealed that the nonequilibrium anisotropic distribution of phonons can endure for 10 ps or longer (*51*). Further thermalization and relaxation of the anisotropic nonequilibrium phonons involve couplings within the monolayer, between the monolayers, and between the HS and the substrate.

To investigate the role of such nonequilibrium phonons in the apparent heating of the adjacent layer (WSe_2), we evaluate the mode-resolved, three-phonon scattering matrix elements by computing the anharmonic, third-order force constants using a supercell approach (*55*) in a commensurate HS with 0° twist angle. We restrict our analysis here to the study of the phonon scattering from $MoSe_2$ to WSe_2 in bilayer $MoSe_2/WSe_2$. This enabled us to determine the characteristic timescales associated with the thermalization of an initially excited phonon in $MoSe_2$. The interfacial phonon-mediated heat transfer will be primarily driven by interlayer phonon-phonon scattering. Therefore, we extract the interfacial scattering processes by calculating the phonon-phonon interlayer matrix elements in a layer-resolved basis using a separable subsystem approach (*56*). Specifically, we compute the coupling between a $MoSe_2$ phonon to any pairs of phonons on $MoSe_2$ and/or WSe_2 by rotating the force constants explicitly computed on the bilayer system onto a product of monolayer phonon basis

(see the Supplementary Materials). Given an initial nonthermal distribution of phonons within the expected wave vector range around K, our calculations demonstrate that the fastest interfacial phonon-phonon scattering events occur within a time range of 15 to 40 ps.

Figure 3D shows a diagram for a representative fast interfacial phonon scattering pathway, in which a $\mathbf{q} \approx K$ phonon in $MoSe_2$ undergoes a fission-like decay into two phonons: a low-energy $\mathbf{q} \approx \Gamma$ phonon in the $MoSe_2$ layer and a high-energy $\mathbf{q} \approx K$ phonon in the WSe_2 layer, transferring energy to the WSe_2 layer. In this representative pathway, the initial $\mathbf{q} \approx K$ phonons within the $MoSe_2$ layer lie on the acoustic branch and show primarily an in-plane chiral motion of the chalcogen atoms and, to a lesser extent, an out-of-plane displacement of the transition-metal atoms (see the Supplementary Materials). We find that such fission-like processes emit a long wavelength acoustic phonon, primarily within the original $MoSe_2$ layer, and an additional higher-energy $\mathbf{q} \approx K$ phonon in the WSe_2 layer. The momentum-resolved scattering-rate associated with such final WSe_2 phonons is shown in Fig. 3F. These larger–wave vector WSe_2 phonons carry most of the energy during the fission of initial $MoSe_2$ phonons, leading to the interlayer thermalization. By integrating the scattering rate over the final distribution of phonons emitted on the WSe_2 layer, we find the fastest (and rate-dominating) channels yield a minimum effective scattering time of $\tau_2^{\text{eff}} \approx 15$ ps, which is in good agreement with our experimental results. Our microscopic analysis also reveals that fast interlayer phonon scattering occurs due to the presence of nearly degenerate phonon modes around $\mathbf{q} \approx K$ on both layers, which can interact via the absorption or emission of low-energy, near-zero momentum, and layer-hybridized acoustic phonons. This three-phonon scattering process is possible in bilayer $MoSe_2/WSe_2$ because the acoustic phonons at the BZ boundary primarily involve the motion of the chalcogen atoms within each monolayer. Hence, the relevant acoustic phonons near $\mathbf{q} \approx K$ on $MoSe_2$ and WSe_2 overlap in momentum and energy (see the Supplementary Materials and fig. S6). In contrast, HSs such as WS_2/WSe_2 studied previously with UED (*40*, *41*, *43*) do not display nearly degenerate phonons near $\mathbf{q} \approx K$ but rather a 30 cm^{-1} energy gap in the relevant ZA modes. The lack of scattering channels may be one reason why the slow rise time constant τ_2 was not previously observed (see the Supplementary Materials).

Compared with interfacial phonon scattering from $MoSe_2$ to WSe_2, we also find the intralayer phonon scattering within the $MoSe_2$ layer is approximately five times faster. However, such intralayer phonon scattering channels involve the emission of $\mathbf{q} \to 0$ phonons with a characteristic root mean square distribution in reciprocal space that is only 3% that of phonons at the BZ edge. Hence, we expect the initial nonthermal distribution of $\mathbf{q} \approx K$ phonons in $MoSe_2$ to be relatively localized in momentum space for a period long enough for the interlayer phonon scattering to take place. We also note that our calculations of nonequilibrium interfacial heat transfer are performed with 0° twist angle. For small but finite twist angles, the formation of large-scale moiré stacking domains likely functions as a stacking fault and serves as phonon scattering centers mimicking the result of the commensurate structure.

DISCUSSION

In conclusion, we have used UED to trace directly the layer-resolved lattice heating dynamics as charge and energy are transferred across vdW interfaces in MoS_2/WS_2 and $WSe_2/MoSe_2$ HSs. Following the fast electron-phonon interactions that heat the lattice on a subpicosecond timescale, interfacial heat transfer occurs on the timescale of tens of picoseconds due to phonon-phonon interactions. The corresponding rate of heat exchange is an order of magnitude faster than that predicted by MD simulations for a fully thermalized model. This difference is attributed to the nonthermal, highly polarized distribution of phonons generated by the initial charge carrier scattering and interlayer CT. Such a nonthermal distribution of phonons leads to a time constant for heat flow within a perturbative theoretical analysis of about 15 ps, comparable to experiment and substantially faster than that for a phonon distribution that is thermalized within a single layer. The interfacial lattice dynamics and the possibility of fast phonon-phonon scattering channels revealed in this work are essential components in the mechanisms of energy transfer in TMDC heterobilayers. This unique mechanism of heat exchange under photoexcited nonequilibrium conditions is of particular interest in the thermal management of the optoelectronic and photonic devices using TMDC HSs in the future.

MATERIALS AND METHODS

Experimental UED setup

Ultrafast pump-probe experiments on the TMDC/TMDC HSs were conducted in the MeV-UED facility at SLAC National Accelerator Laboratory. The femtosecond electron pulses are at normal incidence in a transmission mode geometry. The details on the MeV-UED apparatus can be found elsewhere (*44*, *45*). Electron pulses with 4.2-MeV kinetic energy generated from a photocathode radio-frequency gun were used for the experiment. The MeV electron pulse at the sample position has <150-fs full width at half maximum (FWHM) pulse duration and ~200-μm FWHM spot size. Pump laser pulses near collinearly illuminated the sample together with probe electron pulses. A Ti:sapphire regenerative and multipass amplifier laser system delivers 800-nm laser pulses with 60-fs FWHM pulse duration. Most of the 800-nm laser is used to drive an optical parametric amplifier to generate the resonant pump beam for different TMDC/TMDC HSs. The HSs are cooled down to 40 to 50 K for the cryogenic measurements and 300 K for the room temperature measurements. The diffracted patterns were recorded with a phosphor screen and a lens-coupled ANDOR iXon Ultra 888 electron-multiplying charge-coupled device camera. The pump-probe measurement was performed at a 360-Hz repetition rate. Diffraction images were recorded and averaged at various pump-probe time delays, which provides a high signal-to-noise ratio to perform quantitative dynamics analysis.

Sample preparation

Monolayer samples were prepared using the method of gold tape exfoliation as detailed in (*46*). A 100-nm-thick gold layer is deposited on a flat silicon substrate (NOVA Electronic Materials LLC) via electron-beam evaporation (Kurt J. Lesker LAB 18 e-beam evaporator). A layer of polyvinylpyrrolidone (PVP) solution (Sigma-Aldrich, M_w of 40,000 10 wt % in ethanol/acetonitrile wt 1/1) is spin-coated on top of the Au film (400 rpm, acceleration of 400 rpm/s, 2 min) and cured at 150°C for 5 min as a sacrificial layer to prevent tape residue contamination. The prepared PVP/Au is picked up with thermal release tape (TRT) (Semiconductor Corp.; release

temperature, 90°C), revealing an ultraflat, clean, and fresh gold surface, i.e., the gold tape. The gold tape is pressed onto freshly cleaved bulk MoS_2, WS_2, $MoSe_2$, or WSe_2 single crystals (HQ Graphene). As the tape is lifted off the surface, it carries the PVP/Au layer with a monolayer attached to the Au surface. This is transferred to the 285-nm SiO_2/Si substrate (NOVA Electronic Materials LLC), and the TRT is removed by heating at 95°C. The PVP layer is removed by dissolving it in deionized water via 15 min of continuous stirring. The Au layer is dissolved in a KI/I_2 gold etchant solution [2.5 g of I_2 and 10 g of KI in 100 ml of deionized (DI) water; iodine, 99.99% (Alfa Aesar); and potassium iodide, 99.9% (Alfa Aesar)]. The monolayer is rinsed with DI water and isopropanol and dried with N_2. For stacking heterobilayers, the first layer is prepared on SiO_2/Si. The second layer is exfoliated with a fresh piece of gold tape to obtain the TRT/PVP/Au/monolayer stack and is placed on the first layer at a desired twist-angle. The tape is released, and the heterobilayer then goes through the same rinsing and etching procedure as the first monolayer. The heterobilayers on SiO_2/Si were soaked in acetone for 20 min to 4 hours to promote separation of the TMDC from the substrate before transfer. For transferring onto Si_3N_4 films, a cellulose acetate butyrate (CAB) (Sigma-Aldrich) solution in ethyl acetate was spin-coated on top of the heterobilayer (400 rpm, acceleration of 400 rpm/s, 2 min). The CAB-coated heterobilayer was then dipped in water at a shallow angle, and intercalation of water between the hydrophobic CAB/heterobilayer film and hydrophilic SiO_2/Si substrate released the film from the substrate. The CAB/heterobilayer was then placed on 10- to 15-nm-thick 250 μm–by–250 μm Si_3N_4 membrane windows on Si TEM grids (Ted Pella; TEMWindows). The CAB was dissolved in ethyl acetate, leaving clean monolayer and heterobilayers on the Si_3N_4 film. Two example sample images are shown in fig. S1.

Reflection contrast spectroscopy

To measure the optical absorption of the monolayers, the reflection contrast data were taken with a stabilized Tungsten-Halogen light source (Thorlabs SLS201L, 450 to 5500 nm) focused to ~1 μm on the sample by a 40× objective. The reflected light was then collected by the same objective and measured and analyzed by a Jobin Yvon iHR550 spectrometer equipped with a Synapse CCD camera. All reflection contrast measurements were conducted at ~40 K in a Montana Instrument cryostat. The reflection contrast data were acquired by calculating $(R_{sample} - R_{ref})/R_{ref}$, where R_{sample} is the reflected light spectrum from the sample area and R_{ref} is the reflected spectrum from the TEM grid substrates. The absorption spectra were obtained by fitting the reflection contrast spectra using a transfer matrix method and the RefFit software (*57*).

$MoSe_2/WSe_2$ electronic band structure calculation

The DFT electronic band structure for $MoSe_2/WSe_2$ in the present text is computed with Quantum ESPRESSO, a first-principles DFT, plane-wave–based pseudopotential code (*58*). We consider a $MoSe_2/WSe_2$ HS in the 0° twist angle, R_h^x stacking and use a $6 \times 6 \times 1$ k-point grid with an 80-rydberg energy cutoff and 20 Å of vacuum. We use a Perdew-Burke-Ernzerhof (PBE) exchange-correlation functional (*59*) with a vdW correction "vdw-df-c09x" within the framework of Dion *et al.* (*60*) and Cooper (*61*). We include spin-orbit coupling within a fully relativistic framework in this calculation. The square of this projection is used to color the bands in Fig. 3C.

Thermalized bilayer MD simulations

To compute the heat transport between $MoSe_2$ and WSe_2 assuming a thermalized phonon distribution, we perform classical MD simulations. We construct several $MoSe_2/WSe_2$ lattice configurations with angles between 1° and 27°. For each twist angle, we choose an initial difference in temperatures $\Delta T = T_0^{Mo} - T_0^{W} = 50$ K, where $T_0^{Mo} = 100$ K and $T_0^{W} = 50$ K; these values are chosen to approximate those in the experimental setup when the $MoSe_2$ layer is initially pumped. After a thermalization step of the individual layers, at $t = 0$, we release the two thermostats applied to the individual layers and let the bilayer thermalize as a whole (see Fig. 3E). We fit single exponentials to the rising WSe_2 temperature, T^W, versus time and plot the temperature rise constants τ^W at different twist angles in fig. S5. Further details are discussed in section S2.

First-principles phonon calculation using a perturbation theory approach

To quantify the nonthermal interfacial heat transfer, we use a layer-separable basis approach in which we rotate the phonon-phonon scattering matrix into a basis in which we can directly characterize all phonon modes by layer. We used a similar approach to Ouyang *et al.* (*56*), which calculated the phonon-phonon scattering elements by the off-diagonal components of the bilayer dynamical matrix rotated into a monolayer basis, but we extended this approach here to include the anharmonic effects from three-phonon scattering processes. Further details are discussed in section S3.

Supplementary Materials

This PDF file includes:

Sections S1 to S4
Figs. S1 to S13
Table S1
References

REFERENCES AND NOTES

1. A. K. Geim, I. V. Grigorieva, Van der Waals heterostructures. *Nature* **499**, 419–425 (2013).
2. K. S. Novoselov, A. Mishchenko, A. Carvalho, A. H. Castro Neto, 2D materials and van der Waals heterostructures. *Science* **353**, aac9439 (2016).
3. E. M. Alexeev, D. A. Ruiz-Tijerina, M. Danovich, M. J. Hamer, D. J. Terry, P. K. Nayak, S. Ahn, S. Pak, J. Lee, J. I. Sohn, M. R. Molas, M. Koperski, K. Watanabe, T. Taniguchi, K. S. Novoselov, R. V. Gorbachev, H. S. Shin, V. I. Fal'ko, A. I. Tartakovskii, Resonantly hybridized excitons in moiré superlattices in van der Waals heterostructures. *Nature* **567**, 81–86 (2019).
4. P. Rivera, H. Yu, K. L. Seyler, N. P. Wilson, W. Yao, X. Xu, Interlayer valley excitons in heterobilayers of transition metal dichalcogenides. *Nat. Nanotechnol.* **13**, 1004–1015 (2018).
5. B. Huang, M. A. McGuire, A. F. May, D. Xiao, P. Jarillo-Herrero, X. Xu, Emergent phenomena and proximity effects in two-dimensional magnets and heterostructures. *Nat. Mater.* **19**, 1276–1289 (2020).
6. C.-H. Lee, G.-H. Lee, A. M. van der Zande, W. Chen, Y. Li, M. Han, X. Cui, G. Arefe, C. Nuckolls, T. F. Heinz, J. Guo, J. Hone, P. Kim, Atomically thin p–N junctions with van der Waals heterointerfaces. *Nat. Nanotechnol.* **9**, 676–681 (2014).
7. Y. Liu, N. O. Weiss, X. Duan, H. C. Cheng, Y. Huang, X. Duan, Van der Waals heterostructures and devices. *Nat. Rev. Mater.* **1**, 16042 (2016).
8. C. Jin, E. Y. Ma, O. Karni, E. C. Regan, F. Wang, T. F. Heinz, Ultrafast dynamics in van der Waals heterostructures. *Nat. Nanotechnol.* **13**, 994–1003 (2018).
9. Y. Liu, X. Duan, H.-J. Shin, S. Park, Y. Huang, X. Duan, Promises and prospects of two-dimensional transistors. *Nature* **591**, 43–53 (2021).
10. S.-J. Liang, B. Cheng, X. Cui, F. Miao, Van der Waals heterostructures for high-performance device applications: Challenges and opportunities. *Adv. Mater.* **32**, e1903800 (2020).
11. A. Ciarrocchi, F. Tagarelli, A. Avsar, A. Kis, Excitonic devices with van der Waals heterostructures: Valleytronics meets twistronics. *Nat. Rev. Mater.* **7**, 449–464 (2022).

12. Q. Zeng, Z. Liu, Novel optoelectronic devices: Transition-metal-dichalcogenide-based 2D heterostructures. *Adv. Electron. Mater.* **4**, 1700335 (2018).
13. K. Tran, G. Moody, F. Wu, X. Lu, J. Choi, K. Kim, A. Rai, D. A. Sanchez, J. Quan, A. Singh, J. Embley, A. Zepeda, M. Campbell, T. Autry, T. Taniguchi, K. Watanabe, N. Lu, S. K. Banerjee, K. L. Silverman, S. Kim, E. Tutuc, L. Yang, A. H. MacDonald, X. Li, Evidence for moiré excitons in van der Waals heterostructures. *Nature* **567**, 71–75 (2019).
14. K. L. Seyler, P. Rivera, H. Yu, N. P. Wilson, E. L. Ray, D. G. Mandrus, J. Yan, W. Yao, X. Xu, Signatures of moiré-trapped valley excitons in $MoSe_2/WSe_2$ heterobilayers. *Nature* **567**, 66–70 (2019).
15. P. Rivera, J. R. Schaibley, A. M. Jones, J. S. Ross, S. Wu, G. Aivazian, P. Klement, K. Seyler, G. Clark, N. J. Ghimire, J. Yan, D. G. Mandrus, W. Yao, X. Xu, Observation of long-lived interlayer excitons in monolayer $MoSe_2$–WSe_2 heterostructures. *Nat. Commun.* **6**, 6242 (2015).
16. C. Jin, E. C. Regan, A. Yan, M. I. B. Utama, D. Wang, S. Zhao, Y. Qin, S. Yang, Z. Zheng, S. Shi, K. Watanabe, T. Taniguchi, S. Tongay, A. Zettl, F. Wang, Observation of moiré excitons in WSe_2/WS_2 heterostructure superlattices. *Nature* **567**, 76–80 (2019).
17. K. Tran, J. Choi, A. Singh, Moiré and beyond in transition metal dichalcogenide twisted bilayers. *2D Mater.* **8**, 022002 (2020).
18. D. Huang, J. Choi, C.-K. Shih, X. Li, Excitons in semiconductor moiré superlattices. *Nat. Nanotechnol.* **17**, 227–238 (2022).
19. K. F. Mak, J. Shan, Photonics and optoelectronics of 2D semiconductor transition metal dichalcogenides. *Nat. Photonics.* **10**, 216–226 (2016).
20. E. C. Regan, D. Wang, E. Y. Paik, Y. Zeng, L. Zhang, J. Zhu, A. H. MacDonald, H. Deng, F. Wang, Emerging exciton physics in transition metal dichalcogenide heterobilayers. *Nat. Rev. Mater.* **7**, 778–795 (2022).
21. L. Yuan, B. Zheng, J. Kunstmann, T. Brumme, A. B. Kuc, C. Ma, S. Deng, D. Blach, A. Pan, L. Huang, Twist-angle-dependent interlayer exciton diffusion in WS_2–WSe_2 heterobilayers. *Nat. Mater.* **19**, 617–623 (2020).
22. Y. Zhu, W.-H. Fang, A. Rubio, R. Long, O. V. Prezhdo, The twist angle has weak influence on charge separation and strong influence on recombination in the MoS_2/WS_2 bilayer: Ab initio quantum dynamics. *J. Mater. Chem. A* **10**, 8324–8333 (2022).
23. R. Long, O. V. Prezhdo, quantum coherence facilitates efficient charge separation at a $MoS_2/MoSe_2$ van der Waals junction. *Nano Lett.* **16**, 1996–2003 (2016).
24. Y. Wang, Z. Wang, W. Yao, G.-B. Liu, H. Yu, Interlayer coupling in commensurate and incommensurate bilayer structures of transition-metal dichalcogenides. *Phys. Rev. B.* **95**, 115429 (2017).
25. G. Meneghini, S. Brem, E. Malic, Ultrafast phonon-driven charge transfer in van der Waals heterostructures. *Nat. Sci.* **2**, e20220014 (2022).
26. Q. Zheng, W. A. Saidi, Y. Xie, Z. Lan, O. V. Prezhdo, H. Petek, J. Zhao, Phonon-assisted ultrafast charge transfer at van der Waals heterostructure interface. *Nano Lett.* **17**, 6435–6442 (2017).
27. Q. Zheng, Y. Xie, Z. Lan, O. V. Prezhdo, W. A. Saidi, J. Zhao, Phonon-coupled ultrafast interlayer charge oscillation at van der Waals heterostructure interfaces. *Phys. Rev. B.* **97**, 205417 (2018).
28. Z. Wang, P. Altmann, C. Gadermaier, Y. Yang, W. Li, L. Ghirardini, C. Trovatello, M. Finazzi, L. Duò, M. Celebrano, R. Long, D. Akinwande, O. V. Prezhdo, G. Cerullo, S. Dal Conte, Phonon-mediated interlayer charge separation and recombination in a $MoSe_2/WSe_2$ heterostructure. *Nano Lett.* **21**, 2165–2173 (2021).
29. X.-K. Chen, Y.-J. Zeng, K.-Q. Chen, Thermal transport in two-dimensional heterostructures. *Front. Mater.* **7**, 578791 (2020).
30. Z.-Y. Ong, M.-H. Bae, Energy dissipation in van der Waals 2D devices. *2D Mater.* **6**, 032005 (2019).
31. S. E. Kim, F. Mujid, A. Rai, F. Eriksson, J. Suh, P. Poddar, A. Ray, C. Park, E. Fransson, Y. Zhong, D. A. Muller, P. Erhart, D. G. Cahill, J. Park, Extremely anisotropic van der Waals thermal conductors. *Nature* **597**, 660–665 (2021).
32. B. Amin, N. Singh, U. Schwingenschlögl, Heterostructures of transition metal dichalcogenides. *Phys. Rev. B.* **92**, 075439 (2015).
33. V. O. Özçelik, J. G. Azadani, C. Yang, S. J. Koester, T. Low, Band alignment of two-dimensional semiconductors for designing heterostructures with momentum space matching. *Phys. Rev. B.* **94**, 035125 (2016).
34. X. Hong, J. Kim, S.-F. Shi, Y. Zhang, C. Jin, Y. Sun, S. Tongay, J. Wu, Y. Zhang, F. Wang, Ultrafast charge transfer in atomically thin MoS_2/WS_2 heterostructures. *Nat. Nanotechnol.* **9**, 682–686 (2014).
35. Z. Ji, H. Hong, J. Zhang, Q. Zhang, W. Huang, T. Cao, R. Qiao, C. Liu, J. Liang, C. Jin, L. Jiao, K. Shi, S. Meng, K. Liu, Robust stacking-independent ultrafast charge transfer in MoS_2/WS_2 bilayers. *ACS Nano* **11**, 12020–12026 (2017).
36. V. R. Policht, M. Russo, F. Liu, C. Trovatello, M. Maiuri, Y. Bai, X. Zhu, S. Dal Conte, G. Cerullo, Dissecting interlayer hole and electron transfer in transition metal dichalcogenide heterostructures via two-dimensional electronic spectroscopy. *Nano Lett.* **21**, 4738–4743 (2021).
37. H. Zhu, J. Wang, Z. Gong, Y. D. Kim, J. Hone, X.-Y. Zhu, Interfacial charge transfer circumventing momentum mismatch at two-dimensional van der Waals heterojunctions. *Nano Lett.* **17**, 3591–3598 (2017).
38. E. M. Mannebach, R. Li, K.-A. Duerloo, C. Nyby, P. Zalden, T. Vecchione, F. Ernst, A. H. Reid, T. Chase, X. Shen, S. Weathersby, C. Hast, R. Hettel, R. Coffee, N. Hartmann, A. R. Fry, Y. Yu, L. Cao, T. F. Heinz, E. J. Reed, H. A. Dürr, X. Wang, A. M. Lindenberg, Dynamic structural response and deformations of monolayer MoS_2 visualized by femtosecond electron diffraction. *Nano Lett.* **15**, 6889–6895 (2015).
39. T. L. Britt, Q. Li, L. P. René de Cotret, N. Olsen, M. Otto, S. A. Hassan, M. Zacharias, F. Caruso, X. Zhu, B. J. Siwick, Direct view of phonon dynamics in atomically thin MoS_2. *Nano Lett.* **22**, 4718–4724 (2022).
40. M.-F. Lin, V. Kochat, A. Krishnamoorthy, L. Bassman, C. Weninger, Q. Zheng, X. Zhang, A. Apte, C. S. Tiwary, X. Shen, R. Li, R. Kalia, P. Ajayan, A. Nakano, P. Vashishta, F. Shimojo, X. Wang, D. M. Fritz, U. Bergmann, Ultrafast non-radiative dynamics of atomically thin $MoSe_2$. *Nat. Commun.* **8**, 1745 (2017).
41. D. Luo, J. Tang, X. Shen, F. Ji, J. Yang, S. Weathersby, M. E. Kozina, Z. Chen, J. Xiao, Y. Ye, T. Cao, G. Zhang, X. Wang, A. M. Lindenberg, Twist-angle-dependent ultrafast charge transfer in MoS_2-graphene van der Waals heterostructures. *Nano Lett.* **21**, 8051–8057 (2021).
42. D. Luo, D. Hui, B. Wen, R. Li, J. Yang, X. Shen, A. H. Reid, S. Weathersby, M. E. Kozina, S. Park, Y. Ren, T. D. Loeffler, S. K. R. S. Sankaranarayanan, M. K. Y. Chan, X. Wang, J. Tian, I. Arslan, X. Wang, T. Rajh, J. Wen, Ultrafast formation of a transient two-dimensional diamondlike structure in twisted bilayer graphene. *Phys. Rev. B.* **102**, 155431 (2020).
43. A. Sood, J. B. Haber, J. Carlström, E. A. Peterson, E. Barre, J. D. Georgaras, A. H. M. Reid, X. Shen, M. E. Zajac, E. C. Regan, J. Yang, T. Taniguchi, K. Watanabe, F. Wang, X. Wang, J. B. Neaton, T. F. Heinz, A. M. Lindenberg, F. H. da Jornada, A. Raja, Bidirectional phonon emission in two-dimensional heterostructures triggered by ultrafast charge transfer. *Nat. Nanotechnol.* **18**, 29–35 (2023).
44. S. P. Weathersby, G. Brown, M. Centurion, T. F. Chase, R. Coffee, J. Corbett, J. P. Eichner, J. C. Frisch, A. R. Fry, M. Gühr, N. Hartmann, C. Hast, R. Hettel, R. K. Jobe, E. N. Jongewaard, J. R. Lewandowski, R. K. Li, A. M. Lindenberg, I. Makasyuk, J. E. May, D. McCormick, M. N. Nguyen, A. H. Reid, X. Shen, K. Sokolowski-Tinten, T. Vecchione, S. L. Vetter, J. Wu, J. Yang, H. A. Dürr, X. J. Wang, Mega-electron-volt ultrafast electron diffraction at SLAC National Accelerator Laboratory. *Rev. Sci. Instrum.* **86**, 073702 (2015).
45. X. Shen, R. K. Li, U. Lundström, T. J. Lane, A. H. Reid, S. P. Weathersby, X. J. Wang, Femtosecond mega-electron-volt electron microdiffraction. *Ultramicroscopy* **184**, 172–176 (2018).
46. F. Liu, W. Wu, Y. Bai, S. H. Chae, Q. Li, J. Wang, J. Hone, X.-Y. Zhu, Disassembling 2D van der Waals crystals into macroscopic monolayers and reassembling into artificial lattices. *Science* **367**, 903–906 (2020).
47. S. H. Simon, *The Oxford Solid State Basics* (Oxford Univ. Press, 2013).
48. C. J. R. Duncan, M. Kaemingk, W. H. Li, M. B. Andorf, A. C. Bartnik, A. Galdi, M. Gordon, C. A. Pennington, I. V. Bazarov, H. J. Zeng, F. Liu, D. Luo, A. Sood, A. M. Lindenberg, M. W. Tate, D. A. Muller, J. Thom-Levy, S. M. Gruner, J. M. Maxson, Multi-scale time-resolved electron diffraction: A case study in moiré materials. *Ultramicroscopy* **253**, 113771 (2023).
49. I.-C. Tung, A. Krishnamoorthy, S. Sadasivam, H. Zhou, Q. Zhang, K. L. Seyler, G. Clark, E. M. Mannebach, C. Nyby, F. Ernst, D. Zhu, J. M. Glownia, M. E. Kozina, S. Song, S. Nelson, H. Kumazoe, F. Shimojo, R. K. Kalia, P. Vashishta, P. Darancet, T. F. Heinz, A. Nakano, X. Xu, A. M. Lindenberg, H. Wen, Anisotropic structural dynamics of monolayer crystals revealed by femtosecond surface X-ray scattering. *Nat. Photonics.* **13**, 425–430 (2019).
50. N. R. Wilson, P. V. Nguyen, K. Seyler, P. Rivera, A. J. Marsden, Z. P. L. Laker, G. C. Constantinescu, V. Kandyba, A. Barinov, N. D. M. Hine, X. Xu, D. H. Cobden, Determination of band offsets, hybridization, and exciton binding in 2D semiconductor heterostructures. *Sci. Adv.* **3**, e1601832 (2017).
51. F. Caruso, Nonequilibrium lattice dynamics in monolayer MoS_2. *J. Phys. Chem. Lett.* **12**, 1734–1740 (2021).
52. A. P. Thompson, H. M. Aktulga, R. Berger, D. S. Bolintineanu, W. M. Brown, P. S. Crozier, P. J. In't Veld, A. Kohlmeyer, S. G. Moore, T. D. Nguyen, R. Shan, M. J. Stevens, J. Tranchida, C. Trott, S. J. Plimpton, LAMMPS - a flexible simulation tool for particle-based materials modeling at the atomic, meso, and continuum scales. *Comput. Phys. Commun.* **271**, 108171 (2022).
53. A. Krishnamoorthy, P. Rajak, P. Norouzzadeh, D. J. Singh, R. K. Kalia, A. Nakano, P. Vashishta, Thermal conductivity of MoS_2 monolayers from molecular dynamics simulations. *AIP Adv.* **9**, 035042 (2019).
54. L. Waldecker, R. Bertoni, H. Hübener, T. Brumme, T. Vasileiadis, D. Zahn, A. Rubio, R. Ernstorfer, Momentum-resolved view of electron-phonon coupling in Multilayer WSe_2. *Phys. Rev. Lett.* **119**, 036803 (2017).
55. A. Togo, L. Chaput, I. Tanaka, Distributions of phonon lifetimes in Brillouin zones. *Phys. Rev. B.* **91**, 094306 (2015).
56. W. Ouyang, H. Qin, M. Urbakh, O. Hod, Controllable thermal conductivity in twisted homogeneous interfaces of graphene and hexagonal boron nitride. *Nano Lett.* **20**, 7513–7518 (2020).
57. A. B. Kuzmenko, Kramers–Kronig constrained variational analysis of optical spectra. *Rev. Sci. Instrum.* **76**, 083108 (2005).
58. P. Giannozzi, O. Andreussi, T. Brumme, O. Bunau, M. Buongiorno Nardelli, M. Calandra, R. Car, C. Cavazzoni, D. Ceresoli, M. Cococcioni, N. Colonna, I. Carnimeo, A. Dal Corso,

S. de Gironcoli, P. Delugas, R. A. DiStasio, A. Ferretti, A. Floris, G. Fratesi, G. Fugallo, R. Gebauer, U. Gerstmann, F. Giustino, T. Gorni, J. Jia, M. Kawamura, H.-Y. Ko, A. Kokalj, E. Küçükbenli, M. Lazzeri, M. Marsili, N. Marzari, F. Mauri, N. L. Nguyen, H.-V. Nguyen, A. Otero-de-la-Roza, L. Paulatto, S. Poncé, D. Rocca, R. Sabatini, B. Santra, M. Schlipf, A. P. Seitsonen, A. Smogunov, I. Timrov, T. Thonhauser, P. Umari, N. Vast, X. Wu, S. Baroni, Advanced capabilities for materials modelling with Quantum ESPRESSO. *J. Phys. Condens. Matter* **29**, 465901 (2017).

59. J. P. Perdew, K. Burke, M. Ernzerhof, Generalized gradient approximation made simple. *Phys. Rev. Lett.* **77**, 3865–3868 (1996).
60. M. Dion, H. Rydberg, E. Schröder, D. C. Langreth, B. I. Lundqvist, Van der Waals density functional for general geometries. *Phys. Rev. Lett.* **92**, 246401 (2004).
61. V. R. Cooper, Van der Waals density functional: An appropriate exchange functional. *Phys. Rev. B* **81**, 161104 (2010).
62. A. Togo, I. Tanaka, First principles phonon calculations in materials science. *Scr. Mater.* **108**, 1–5 (2015).
63. J.-W. Jiang, Parametrization of Stillinger–Weber potential based on valence force field model: Application to single-layer MoS_2 and black phosphorus. *Nanotechnology* **26**, 315706 (2015).
64. M. H. Naik, I. Maity, P. K. Maiti, M. Jain, Kolmogorov–Crespi potential for multilayer transition-metal dichalcogenides: Capturing structural transformations in moiré superlattices. *J. Phys. Chem. C* **123**, 9770–9778 (2019).
65. A. Togo, First-principles Phonon Calculations with Phonopy and Phono3py. *J. Physical Soc. Japan* **92**, 012001 (2023).
66. A. Cepellotti, J. Coulter, A. Johansson, N. S. Fedorova, B. Kozinsky, Phoebe: A high-performance framework for solving phonon and electron Boltzmann transport equations. *J. Phys. Mater.* **5**, 035003 (2022).
67. A. Sood, F. Xiong, S. Chen, R. Cheaito, F. Lian, M. Asheghi, Y. Cui, D. Donadio, K. E. Goodson, E. Pop, Quasi-ballistic thermal transport across MoS_2 thin films. *Nano Lett.* **19**, 2434–2442 (2019).
68. H. L. Zhuang, R. G. Hennig, Computational search for single-layer transition-metal dichalcogenide photocatalysts. *J. Phys. Chem. C* **117**, 20440–20445 (2013).

Acknowledgments: F.L. thanks X. Wang's support on the UED sample screening. **Funding:** F.L. acknowledges support from a Terman Fellowship and startup funds from the Department of Chemistry at Stanford University. Theoretical and computational work was supported by the National Science Foundation CAREER award through grant no. DMR-2238328. T.F.H., A.M.L., D.L., A.S., and H.Y. acknowledge support at SLAC from the Department of Energy, Office of Basic Energy Sciences, Division of Materials Sciences and Engineering, under contract DE-AC02-76SF00515 for the UED measurements, optical characterization, and analysis. Part of this work was performed at the Stanford Nano Shared Facilities (SNSF), supported by the National Science Foundation under award ECCS-2026822. The MeV-UED experiments were carried out at SLAC MeV-UED, U.S. Department of Energy Office of Science User Facilities, operated as part of the Linac Coherent Light Source at the SLAC National Accelerator Laboratory, supported by the U.S. Department of Energy, Office of Science, Office of Basic Energy Sciences under contract no. DE-AC02-76SF00515. This research used resources of the National Energy Research Scientific Computing Center (NERSC), a U.S. Department of Energy Office of Science User Facility located at Lawrence Berkeley National Laboratory, operated under contract no. DE-AC02-05CH11231 using NERSC award BES-ERCAP m3606 for the MD simulations, and from the Texas Advanced Computing Center (TACC) at The University of Texas at Austin, funded by the National Science Foundation (NSF) award 1818253, through allocation DMR21077 for the calculations of the phonon-phonon scattering matrix elements. J.D.G. acknowledges support from the Natural Science and Engineering Research Council (NSERC) Canada through the Post-Graduate Scholarship PGS D-568202-2022. **Author contributions:** F.L. and A.M.L. conceived and supervised the project. D.L. and X.S. designed the experiments. F.H.d.J. designed the theoretical and computational approaches. A.C.J. prepared the sample with the support of F.L. J.D.G. conducted the MD simulations with the support of F.H.d.J. A.C.J., X.S., H.J.Z., A.P.S., and H.K. performed the UED experiments. A.C.J. and H.Y. performed the reflection spectroscopy measurements with the support of T.F.H. A.C.J. analyzed the data. A.S. assisted in the interpretation of results. All authors have read and edited the manuscript. **Competing interests:** The authors declare that they have no competing interests. **Data and materials availability:** All data needed to evaluate the conclusions in the paper are present in the paper and/or the Supplementary Materials.

Submitted 21 July 2023
Accepted 22 December 2023
Published 24 January 2024
10.1126/sciadv.adj8819